IEEE Access
Multidisciplinary | Rapid Review | Open Access Journal

Received 31 July 2022, accepted 9 August 2022, date of publication 16 August 2022, date of current version 24 August 2022.

Digital Object Identifier 10.1109/ACCESS.2022.3199002

RESEARCH ARTICLE

Focused Planar Electromagnetic Waves for Enhanced Near-Field Microwave Imaging With Verification Using Tapered Gradient-Index Lens Antenna

AZIN S. JANANI, AMIN DARVAZEHBAN, (Member, IEEE), SASAN AHDI REZAEIEH, (Member, IEEE), AND AMIN M. ABBOSH, (Fellow, IEEE)
School of Information Technology and Electrical Engineering, The University of Queensland, Brisbane, QLD 4072, Australia

Corresponding author: Azin S. Janani (azin.janani@uq.edu.au)

The work of Amin Darvazehban was supported in part by EMvision Med Tech, Australia.

ABSTRACT Radar-based algorithms for electromagnetic (EM) imaging are developed based on the assumption that EM has a local planar wave front inside the imaging domain. However, this might not be the case for majority of utilized antennas as the imaged object is usually located within the near-field zone of the antenna. The impact of that assumption on imaging accuracy and whether utilizing an antenna that can create a focused planar wave front inside the imaging domain improves EM imaging are investigated in torso imaging as an example. Thus, three types of antennas are used to scan the torso; 1) bio-matched loop-dipole, 2) Gradient-Index lens (GRIN), and 3) Tapered GRIN (T-GRIN) lens antenna. The proposed T-GRIN lens antennas is designed to create a focused plane wave propagation inside the torso using tapered trapezoid water-filled cavities inside a host medium. The proposed design improves penetration depth by 33% compared to conventional GRIN lens and 75% compared to the bio-matched loop-dipole antenna, in a wide fractional bandwidth of 83% at 0.7-1.7 GHz. The realized results indicate that generating focused plane wave inside the imaged object, which is realized using T-GRIN lens antenna, improves the detection accuracy by 15 % and 56% compared to conventional GRIN lens and bio-matched loop-dipole antennas, respectively. Moreover, the localization accuracy is improved by 54.5% and 100% compared to conventional GRIN lens and bio-matched loop-dipole antenna, respectively. This study highlights the importance of creating focused planar wave front within the imaging domain for improved detection and localization using microwave techniques.

INDEX TERMS Antenna, focused planar wave, radar-based imaging, near-field microwave imaging.

I. INTRODUCTION

During past decades, research effort in advancement of biomedical imaging modalities has led to the development of many electromagnetic (EM) medical imaging systems [1], [2], [3], [4], [5], [6], [7], [8], [9], [10], [11], [12]. These novel modalities aim at complementing or addressing shortcomings of traditional systems by their non-ionizing radiations, portability, and low cost. The developed EM systems have demonstrated promising attributes in detection and localization of breast cancer [1], [7], [8], [9], 10], brain tumor and stroke [6], plural effusion and pulmonary edema [2], [13], lung cancer [3], [4], [5] by utilizing the dielectric contrast between healthy and unhealthy tissues.

Thoracis diseases are significant contributors to the world's mortality rate [14]. For example, pleural effusion and pulmonary edema are the common initial symptom of many devasting diseases including, lung and breast cancers, and heart failure. Hence, the potential of torso EM imaging in the early detection of accumulated fluid will enable early diagnosis of the underlying life-threatening disease.

EM imaging systems are generally composed of two main parts: 1) hardware (antennas, transceivers, and processing unit), and 2) software (imaging algorithms). The

The associate editor coordinating the review of this manuscript and approving it for publication was Ravi Kumar Gangwar.

core element of the hardware is the antenna that transmits EM signals towards the imaging domain and receives backscatter/reflected signals. EM imaging algorithms are categorized into two main groups that are radar-based and tomography algorithms. Radar based techniques use delay-and-sum [1], [3], [6], [7], beamforming [8], [9], [10], or frequency-based techniques [11], whereas tomography utilizes optimization-based methods [15], [16], Born iterative process [12], or Newton-based techniques [17], [18]. These algorithms generally suffer from high computation cost due to their iterative regularization approach needed to deal with such an ill-posed problem [19].

Generally, radar-based imaging algorithms rely on the assumption of a plane wave radiation of the imaged object in their processing [1], [3], [6], [7], [8], [9], [10]. However, most of medical imaging systems use bio-matched antennas, which create spherical wave radiation in the imaging domain located in their near-field zone [20], [21], [22], which results in non-accurate target detection and localization. The problem is that the imaging domain is located at the near-field of generally designed antennas, but the utilized algorithms assume a far-field approximation and thus a local planar wave within that domain. To tackle this, the imaging antennas might be moved away from the imaging domain, herein they are named free-space antennas, so that the domain is located in the far-field zone of the antenna and thus the EM wave in that domain will be planar [13], [23]. However, that solution causes low penetration depth, serious clutter and low signal-to-noise ratio due to strong skin-interface reflections. To enhance penetration, metasurfaces and high-impedance surfaces can be used [24], [25]. However, they still suffer from strong skin interface reflections. The other solution is re-designing the antennas so that they can have planar wave at their near field zone by incorporating gradient-index (GRIN) lens structure, which transforms spherical incident wave into plane wave in the near-field zone [26], [27], [28], [29]. Generally, GRIN lenses are formed based on multilayer dielectric structures to attain planar waves at the desired location using (1) metamaterial structures [27], (2) drilling holes inside high/low-dielectric host materials [28], and (3) 3-D printing layers [29]. 3-D printing technology significantly help in attainting the required dielectric values by providing an additional degree of freedom in creating different shapes and hole sizes [30], [31]. The application of GRIN lens structure in body-matched configuration for near-field microwave imaging was first investigated in [26]. It is shown that bio-matched GRIN lens improves imaging to some extent. To further enhance EM imaging, a focused planar incident field with high penetration depth inside the imaging domain is required. Thus, a tapered GRIN (T-GRIN) lens is proposed and utilized in torsos imaging as an example. The focused planar incident field results in improvement in detection by reducing the effect of undesired scatterers. The effect of focused incident field in microwave imaging has been investigated in [32], [33] concerning the importance of focused incident field on quality of tomography images in a simulated setup, without using real-life antennas. The distribution of the simulated wave in that study was varied by changing the mathematical simulated model. However, the creation of a focused incident field in a real scenario by designing a proper antenna is still a research question. Also, the effect of focused incident field with planar wavefront in radar-based imaging is another research question.

In this paper, the effect of enhanced penetration depth associated with planar wave propagation on the accuracy of imaging in pulmonary edema detection is investigated. To do this, the accuracy and quality of the obtained images in three experimental setups are evaluated. These setups utilize a 3-D printed multi-layer torso phantom and different antenna types to create three distinct scenarios: 1) Spherical incident field distribution with medium penetration depth using a body-matched loop-dipole antenna, 2) plane wave incident field with high penetration depth by incorporating a GRIN lens to a slot radiator, and 3) focused plane wave incident field using the tapered GRIN (T-GRIN) lens, which has 30% wider impedance bandwidth and 33% higher penetration depth compared to GRIN lens. The frequency-domain confocal Delay-Multiply-And-Sum (DMAS) [1] is used to evaluate the performance of each antenna. Phase alignment and pairing circular convolutions of S-parameters in frequency domain, which are equivalent to time alignment and pairing multiplications of signals in time domain, are utilized. To have a fair comparison between antennas, the same frequency bandwidth is used. Three quantitative metrics (average target to clutter ratio, maximum target to clutter ratio, and actual to detected targets distance) are used to assess target detection and localization in each setup. The results indicate an average improvement by 37.6% in detection and more than 54.5% in localization using T-GRIN lens design compared to others. The results confirm the importance of realizing a focused planar incident field in EM medical imaging.

II. SYSTEM CONFIGURATION

A. UTILIZED ANTENNAS

To investigate the impact of enhanced penetration depth and local planar wavefronts in the near field zone of the antenna on EM medical imaging system, fluid accumulated detection and localization inside the lungs is used as an example. Three different experimental setups are designed. The experimental setup is depicted in Fig. 1(d) and the details of each setup are shown in Fig. 1(a)-(c). The impedance matching characteristic of the utilized antennas in front of the human torso model is depicted in Fig. 2. The reflection coefficients ($|S_{11}|$) of the utilized antennas in front of a human torso model is derived using CST Microwave Studio. The model consists of skin (2 mm), fat (8 mm), muscle (15 mm), and average torso (250 mm). The dispersive dielectric properties of each tissue are obtained from IT'IS [34]. The bio-matched antennas (bio-matched loop-dipole, GRIN lens and T-GRIN lens) are attached to the torso. To avoid any airgap between the antennas and the torso model, a coupling medium

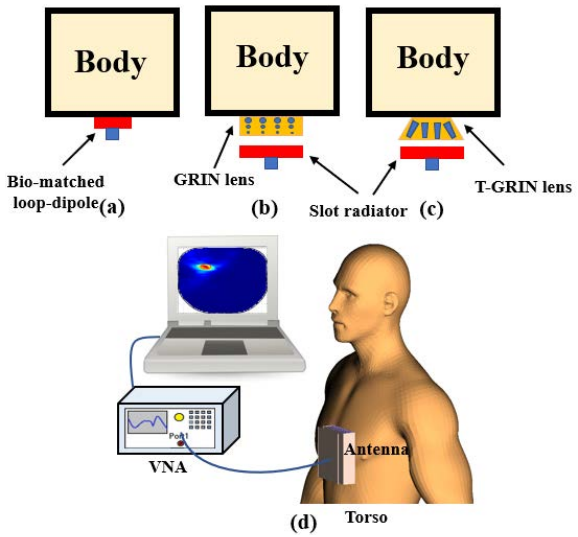

FIGURE 1. Schematic of the (a) bio-matched loop-dipole, (b) GRIN lens, (c) T-GRIN lens antennas, and (d) system configuration. All antennas are placed on to the body.

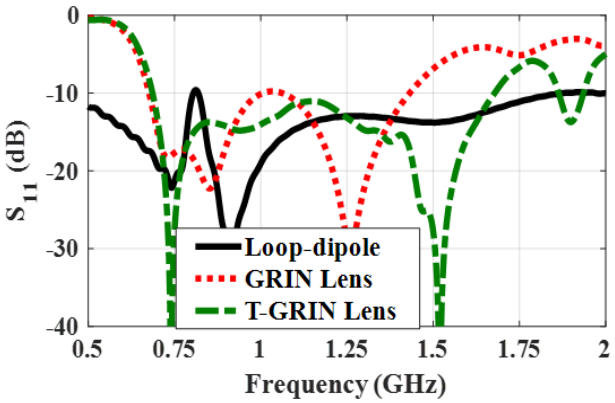

FIGURE 2. Comparison of simulated $|S_{11}|$ between loop-dipole, GRIN lens and T- GRIN lens antennas.

with dielectric property of an average torso, permittivity of 45.3 and conductivity of 0.97, is used. Based on Fig. 2, the operation bandwidth of T-GRIN lens is 0.7-1.7 GHz, which is wider than the traditional GRIN lens design, 0.7-1.4 GHz. The setup (Fig.1) and relevant reflection coefficients (Fig.2) are thoroughly discussed hereafter.

The first setup utilizes a bio-matched loop-dipole antenna (Fig. 1(a)). This antenna utilizes the concept of loop-dipole combination to enhance the signal penetration into the human body [35]. It is designed in the presence of average human torso to operates at 0.5-1.8 GHz (Fig. 2). However, it usually creates a spherical wavefront in the investigation domain. To tackle the limitation of loop-dipole antenna, bio-matched GRIN lens antenna is used in the second setup to transform spherical incident wave into a plane wave inside the torso [26]. It should be noted that the GRIN lens antenna aims to transfer the far-field zone to be within the imaged domain to enable creating a local planar wave front for an accurate near-field radar-based imaging. The proposed design utilizes a H-slot antenna as the radiating element and incorporates a body matched GRIN lens to enhance the penetration and increase the bandwidth at 0.7-1.4 GHz (Fig. 1 (b)). To create a focused planar incident field with high penetration depth inside the torso, modified version of GRIN lens (T-GRIN) is utilized in the third setup. This design can further enhance the impedance bandwidth at 0.7-1.7 GHz (Fig. 1(c)). The focused planar incident field results in reducing the undesired scattering from unwanted scatterers in the imaging domain and improving the detection accuracy [33]. This will thoroughly be investigated in Sec IV.

Details of the bio-matched loop-dipole and GRIN lens structure are thoroughly presented in [35] and [26], respectively. For a fair comparison, the common frequency bandwidth of 0.8-1.2 GHz is used in all setups (Fig. 2). This frequency band is shown to achieve the best compromise between wave penetration into the image domain, antenna's dimension, and resolution of the obtained images [13].

B. T-GRIN LENS DESIGN

The conventional bio-matched GRIN lens is designed based on the theory of multilayer reflection [26], [36]. Four layers of water-filled cylindrical holes with incremental radii are inserted into a host medium with low permittivity to gradually transform the wave impedance from air to torso area [26]. As discussed in [26], by increasing number of layers, the wave transition and the EFI values are improved. However, further increase in number of layers does not provide any additional improvement in the results. In the modified version of the GRIN lens, multiple sets of cylindrical holes have been replaced with trapezoid type cavities inside the host medium to form different matching layers. The cavities are filled with distilled water ($\varepsilon_r = 79$ at 1 GHz) and the host medium that is the 3-D printed is made of Polylactic Acid, which has a measured dielectric constant (ε_r) of 2.5 at 1 GHz. Since this 3D printed material is only used as a thin mold to host the main material, i.e. water, it does not affect the design. The width of the trapezoid is gradually increasing from x_1 to x_2 (see Fig. 3), and hence the effective permittivity of the GRIN lens is gradually increasing. The effective permittivity of the structure can be approximated by [37]:

$$\varepsilon_{eff} = \varepsilon_{water} v_1 + \varepsilon_{host} (1 - v_1) \quad (1)$$

where v_1 is the volume fraction of the water in the host domain. As seen in Fig. 3(b), by increasing width of the trapezoid from air toward human torso, the volume fractional of water enhances. As a result, the effective permittivity of the structure gradually matches to the impedance of the torso. This approach has several advantages compared to the multi-layer cylindrical holes GRIN lens presented in [26]. The trapezoid cavities offer more degree of freedom in incrementally increasing the dielectric property of the GRIN lens instead of restraining the design to a limited number of layers. This results in a widened bandwidth compared

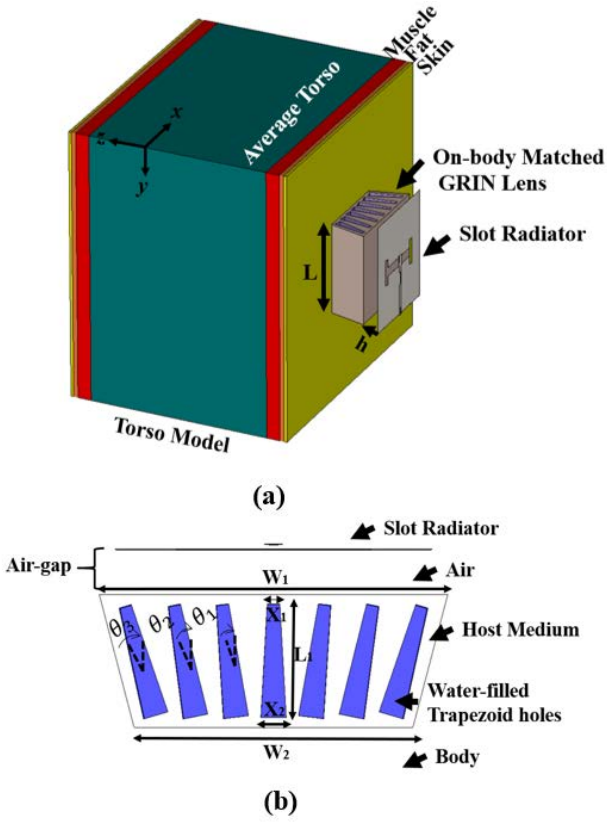

FIGURE 3. (a) 3D configuration of the T- GRIN lens on a torso model, and (b) cross-sectional T-GRIN lens configuration, L=100 mm, h=10 mm, W1= 120 mm, W2= 90 mm, L1= 30 mm, X1= 4 mm, X2= 8 mm, $\theta 1 = 100$, $\theta 2 = 200$, $\theta 3 = 300$.

to traditional GRIN lens. As seen in Fig. 2, T-GRIN lens improves impedance matching by 30%. Moreover, the presented design creates a focused plane wave inside the imaging domain. To increase the penetration depth, the trapezoid cavities are rotated across the center by incremental angles of 10^0. Fig. 4 illustrates the power flow inside the cavities at a sample frequency of 0.9 GHz. As seen, by rotating the cavities the energy traps inside the cavities and converges toward the center of the lens structure. As a result, a focused near field distribution with high penetration depth can be achieved inside the imaging domain. Investigating different rotation angles reveal that further increase in the rotation angle does not improve the penetration depth due to the fact that the inclined cavities cannot be excited using the slot radiator. Moreover, using tapered trapezoid host medium instead of a rectangular one reduces the total area of the lens by 47%.

The initial design parameters are selected based on the GRIN lens design method presented in [26]. The final dimensions of the GRIN lens, presented in the caption of Fig. 3, are achieved using Particle Swarm Optimization method (PSO) in CST Microwave Studio for minimum reflection and enhanced penetration. Finally, the lens is fabricated using 3D printing technology.

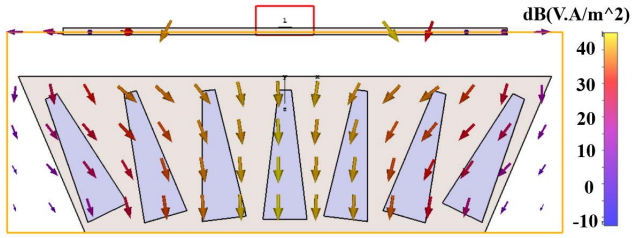

FIGURE 4. Power flow inside the lens cavities at sample frequency of 0.9 GHz.

C. EFFECT OF DESIGN PARAMETERS

The effect of different design parameters on the performance of the proposed T-GRIN lens antenna is studied by changing only one parameter at each investigation.

1) ANTENNA AND LENS SPACING

One of the factors affecting the performance is the spacing between the antenna and the lens. This space is optimized for a maximum field at the center of the torso. As shown in Fig. 5(a), decreasing and increasing this distance adversely affect the impedance matching at frequencies between 0.75 GHz and 1.1 GHz. This mismatch can also be observed from EFI values of the antenna at different distances as shown in Fig. 5(b). Those results are consistent with the observations in [26].

2) THICKNESS OF THE LENS

The reflection coefficients and EFI values of proposed T-GRIN lens antenna with different thickness of lens layer are investigated. As shown in Fig. 6(a), reducing the thickness of the lens structure has an adverse effect on the impedance matching and resonance peaks of the antenna at 0.75 and 1.4 GHz. This is due to incorrect impedance transformation of the torso as seen by the antenna across the free space at lower thickness of the lens. However, increasing the thickness of the lens from 25 mm to 30 mm results in a wide impedance matching due to improved impedance transformation and enhanced wave transition. This outcome is also evident from EFI values of the antenna with different lens thicknesses as shown in Fig. 6(b). By decreasing the lens thickness, the peak of EFI value is decreased. However, increasing the lens thickness beyond an optimal point (30 mm) does not improve the results. The observed effects of lens thickness in T_GRIN lens antenna is consistent with the effect of lens layers in conventional lens design as discussed in [26].

D. THE NEAR-FIELD ELECTRIC FIELD DISTRIBUTION OF THE UTILIZED ANTENNAS

To elaborate on the forestated notions, the near-field incident electric field distribution of each antenna inside a numerical model of human torso with the average depth of 250 mm is examined at a sample frequency of 0.9 GHz and depicted in Fig. 7. As seen, the field distribution of bio-matched loop-dipole antenna has a local spherical wavefront in the

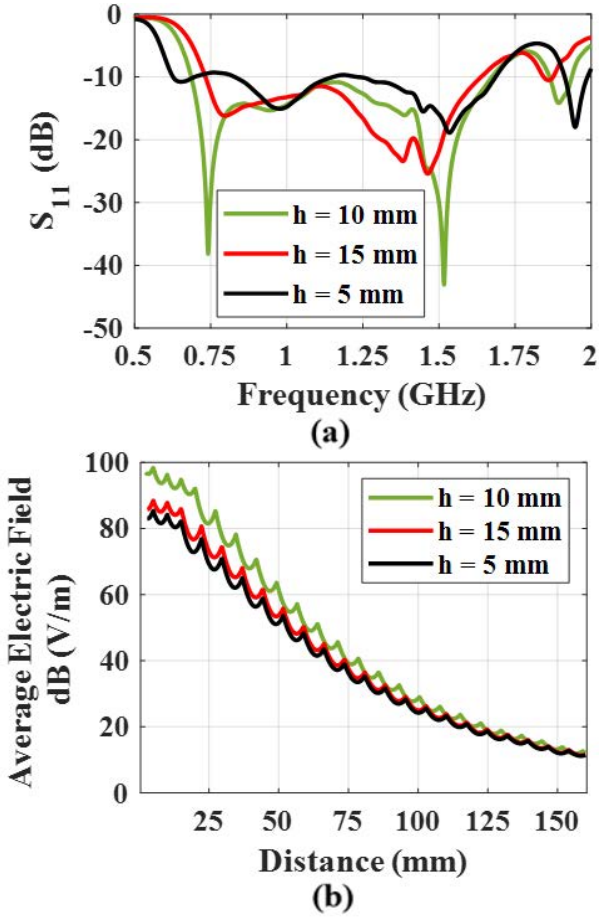

FIGURE 5. Effect of changing spacing between the antenna and the lens. (a) S_{11} and (b) EFI value at 0.9 GHz.

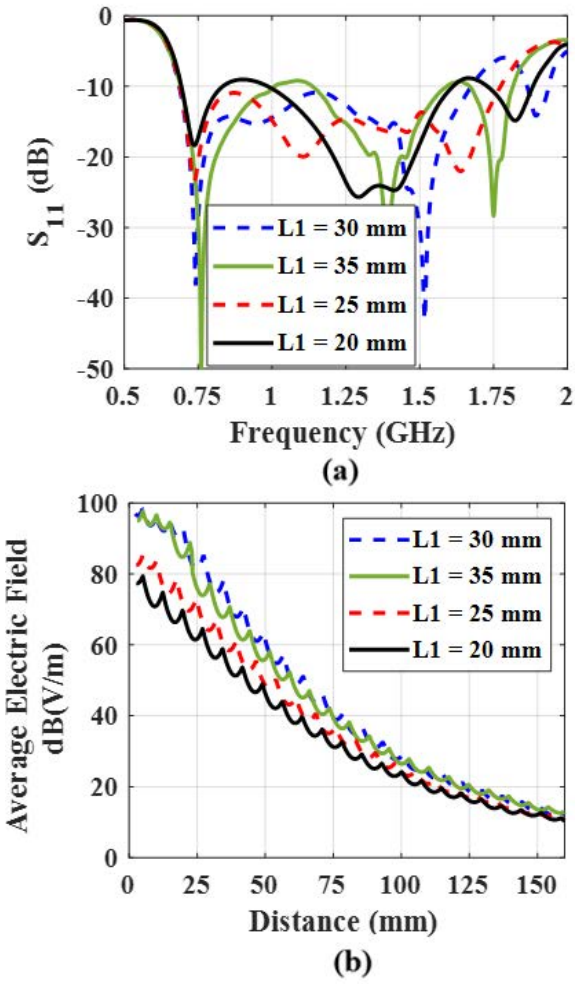

FIGURE 6. Effect of changing the thickness of the lens. (a) S_{11} and (b) EFI value at 0.9 GHz.

investigation domain, which spread out in the direction transverse to radiation direction (specified by dashed lines). As a result, the penetration depth is only 50 mm (Fig. 7(a)). Incorporating the GRIN lens transforms the spherical wave to plane wave (Fig. 7(b)). The T-GRIN Lens design leads to a more focused plane wave with higher penetration depth than conventional GRIN lens design (Fig. 7(c)). The penetration depth improves by 33% compared to conventional GRIN lens and 65% compared to bio-matched loop-dipole. Further analysis regarding the effect of incident field on the imaging quality will be discussed in Sec IV.

III. IMAGING ALGORITHM AND QUANTITATIVE METRICS

To evaluate the effect of wave propagation type on the quality of EM imaging, the frequency-domain confocal Delay-Multiply-And-Sum (DMAS) [1] imaging method is utilized. Fig. 8 depicts the block diagram of the imaging algorithm. Firstly, the difference of measured back-scattered signals from two scanned scenarios, non-homogenous medium with the presence of target (S^p) and homogenous medium with the absence of the target (S^a), are calculated to form the calibrated signals. To mitigate surface/ interface strong reflections, the average of all signals is subtracted from each signal. Using a background homogenous reference is challenging, due to the impact of any significant contour differences between the reference homogeneous model and tested mode, but feasible as proven in some clinical results [38], [39]

Secondly, at each location inside the torso (x, y), the calibrated signals are aligned based on the round-trip distance (r) from the location of the antenna to the scatterer and their amplitude is compensated according to the distance dependency of the plane wave as:

$$A_i(f, (x, y)) = S_i^c(f)\frac{e^{-ikr(x,y)}}{r} \tag{2}$$

where k is the average wavenumber of the imaging domain. It should be noted that average permittivity of 45 (the average permittivity of torso tissues at mid frequency band, 1 GHz) is used to find the value of k. Thirdly, pairing circular convolutions (equivalent to time-domain multiplication) of aligned signals are performed to suppress clutters. Finally, the intensity value at the point scatterer is obtained by adding the

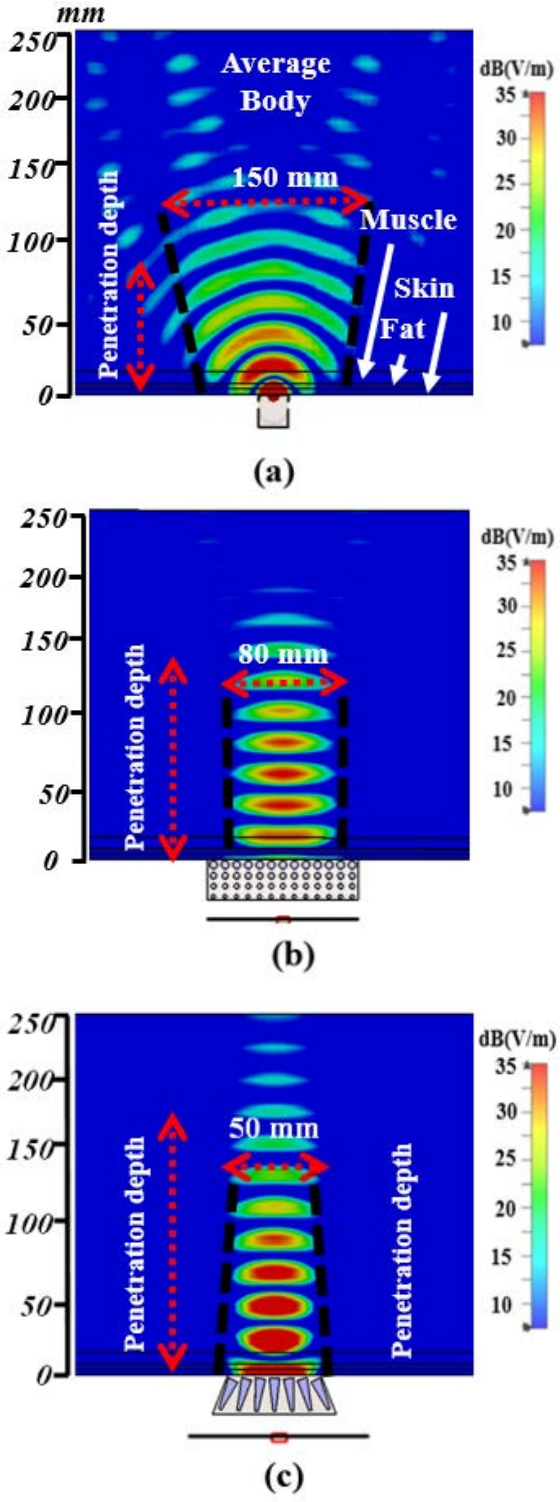

FIGURE 7. Electric field distribution of (a) bio-matched loop-dipole, (b) GRIN lens, and (c) T-GRIN lens at 0.9 GHz.

contributions of all signals over the frequency band as:

$$I(x,y) = \left| \sum_{f=1}^{N_f} \left(\sum_{i=1}^{N_a} \sum_{j=i+1}^{N_a-1} A_i(f,(x,y)) * A_j(f,(x,y)) \right) \right| \quad (3)$$

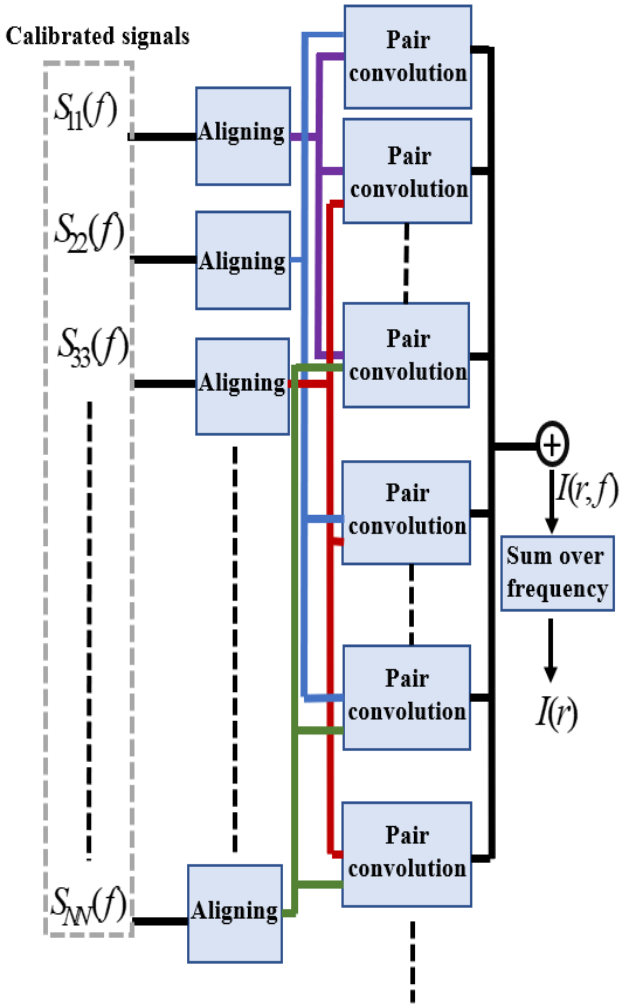

FIGURE 8. Block diagram of the imaging algorithm to obtain intensity at location *r* within the imaging domain.

where N_a and N_f defines the number of antennas and frequency samples, respectively. Intensity values will be higher at the location of the target due to the high dielectric contrast between the target (pathology) and healthy tissues.

To assess the obtained images, three quantitative metrics are used. The first one calculates the average target to clutter ratio [6]:

$$Q = \frac{mean(I(p))}{mean(I(q))}, \quad p \in T,\ q \in S,\ q \notin T \quad (4)$$

where T and S determine the areas correspondent to the target and the rest of the imaging domain, respectively. The higher value of Q means higher average target-to-clutter ratio. The second function calculates the accuracy of detection by measuring the maximum target to clutter ratio [6]:

$$\gamma = \frac{max(I(p))}{max(I(q))}, \quad p \in T,\ q \in S,\ q \notin T \quad (5)$$

an accurate target detection results in $\gamma > 1$, while wrong detection results in $\gamma \leq 1$. A clutter as strong as the target

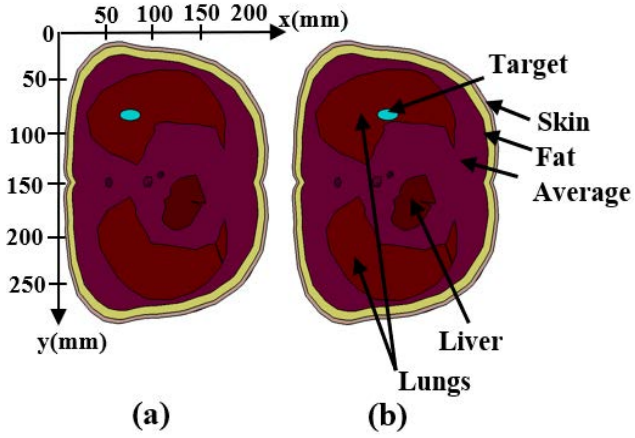

FIGURE 9. Numerical model of torso with lungs, liver, fat, and skin with (a) shallow, and (b) deep targets.

TABLE 1. The dielectric property of tissues At 1 GHz.

TISSUE TYPE	Relative permittivity/Conductivity
Skin	40.9/0.89
Fat	5.4/0.05
Muscle	54.8/0.97
Spleen	56.6/1.32
Inflated lung	21.8/0.47
Liver	46 /0.89
Average	45.3/0.97

results in $\gamma = 1$. The last function calculates the accuracy of localization by measuring the distance between the centers of the detected and the actual targets [6]:

$$\Delta = \|C_{detected} - C_{atual}\| \tag{6}$$

More accurate localization results in lower value of Δ.

IV. SIMULATED AND EXPERIMENTAL EVALUATION

In this section, the effect of wave propagation type and penetration depth on target detection and localization is evaluated using simulated and measured signals.

A. SIMULATED SCENARIO

The realistic 3-D numerical torso in CST Microwave Studio is used for simulation. This model is based on MRI scan from virtual populations models (ViP) [35]. As shown in Fig. 9, this model consists of realistic lungs, liver, fat, and skin layers. The dispersive dielectric property (permittivity and conductivity) of these tissues is set based on IT IS [34]. The area between lungs and liver is represented by the average dielectric property of different torso tissues (muscle, inflated lung, liver, and spleen). Table 1 shows the dielectric properties of different tissues at 1 GHz.

Each of the utilized imaging antenna types is rotated around the torso with 18° step intervals. The minimum step

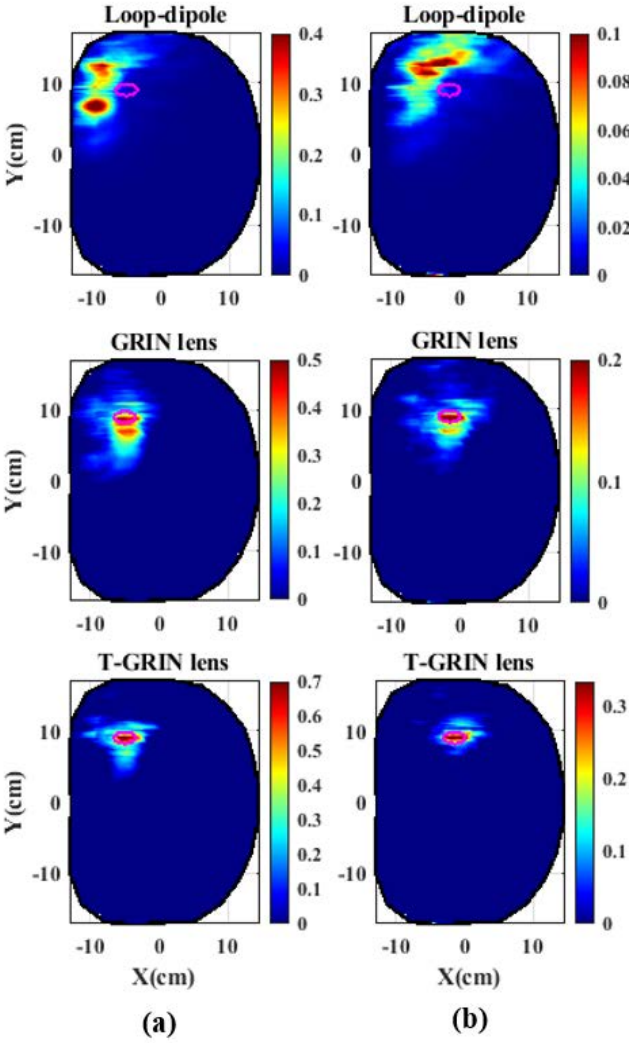

FIGURE 10. Generated images from different antennas of the numerical torso with (a) shallow and (b) deep targets.

interval for scanning the torso is obtained based on the degree of freedom (DOF) theory [40]. Based on this theory, to achieve an accurate target detection, the perimeter of the torso should be sampled at a minimum rate equal to half of the wavelength of transmitted wave [41]:

$$\Delta\phi \leq \frac{\lambda_{min}}{2a} \tag{7}$$

where a is the perimeter of the torso. For the investigated scenario, the torso should be sampled by $\Delta\phi \leq 0.32$ *rad* or 18.23°. Decreasing step interval below this value increases the scanning time without improving the detection accuracy.

This process is repeated for all three antennas (loop-dipole, GRIN lens, and T-GRIN lens). A matching medium with the dielectric property of the average torso is placed between each antenna and the hard-shell of the phantom to avoid any air-gap that may adversely affect signal penetration from those antennas. As shown in Fig. 9, a target, which is an elliptical volume of distilled water (10 ml), is placed at the

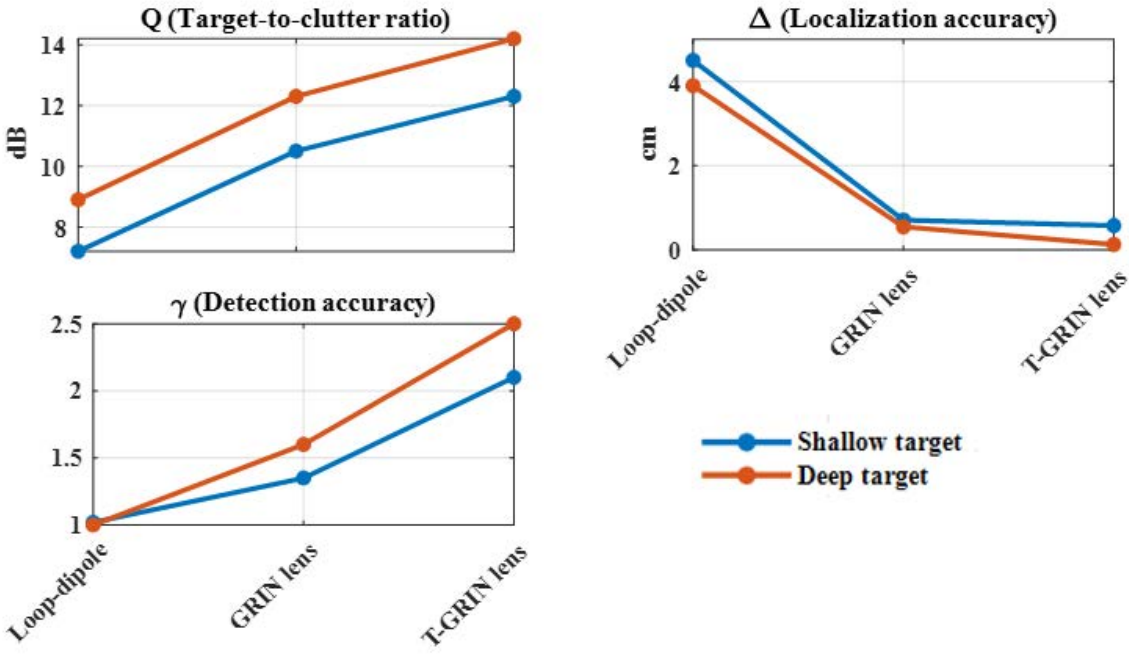

FIGURE 11. Quantitative analysis of the obtained images using different antennas.

bottom of right lung at shallow and deep positions to mimic pulmonary edema condition. For shallow position, the target is located further away from the skin surface at depth x = 75 mm and y = 75 mm. For deep position, the target is located in the middle of the lung at depth x = 110 mm and y = 75 mm.

Fig. 10 illustrates the obtained images of the torso using DMAS for the data collected from the three different antennas. Each image is scaled up to its maximum scattered field intensity. This assists in comparing the level of calculated intensity field within the imaging domain in different setups, which also reflects the penetration depth achieved by each antenna. Visual inspection determines that obtained images using T-GRIN lens antenna have the highest level of intensity within the imaging domain as the propagated wave into the torso achieves the highest penetration depth compared to other antennas, Fig. 7(c). Additionally, the quality of the obtained images is slightly lower for the shallow target due to the resultant of the reflected and trapped incident field between different surface layers of the torso [42]. This strong surface reflections usually mask the weak back-scattered signals from the shallow target. It should be noted that the utilized calibration technique could not completely remove these strong reflections due to variation in thickness of the fat layer around torso.

To verify these observations, the obtained images are analysed using three quantitative metrics, and the results are presented in Fig 11. In deep target scenario, the average target to-clutter-ratio obtained by T-GRIN lens setup is better by 15.4% and 59% than GRIN lens and bio-matched loop-dipole setups, respectively. Additionally, its detection accuracy is better by 39.4 % and 85.1% than GRIN lens and bio-matched loop-dipole setups, respectively.

In shallow target scenario, T-GRIN lens setup achieves 17% and 68% higher target-to clutter-ratio and 54%, and 95% better detection accuracy than GRIN lens and bio-matched loop-dipole setups, respectively. Additionally, in both scenarios, T-GRIN lens and GRIN lens antennas localize the target within 5.5 mm and 8 mm, respectively. However, the localization error of bio-matched loop-dipole is more than 20 mm. Hence, the T-GRIN lens design results in enhanced localization accuracy. According to that, the utilized antennas for scanning the torso can be ranked based on their detection and localization accuracy (image quality) as: 1) T-GRIN lens, 2) GRIN lens, and 3) bio-matched loop-dipole.

The poor performance of bio-matched loop-dipole might be the resultant of its spherical wave radiation that cannot fulfil the assumption of a plane wave distribution inside the imaging domain as needed by the imaging algorithm. As the structure of GRIN lens antennas create plane wave incident field distribution with higher penetration depth inside the imaging domain, the quantitative accuracy of their obtained images is enhanced compared to bio-matched loop-dipole antenna. However, higher average target-to-clutter ratio and detection accuracy of the T-GRIN lens setup in both scenarios (deep and shallow target location) contributes to its focused high intensity incident field distribution. This can suppress scattering signals from undesired surrounding tissues and hence, increase detection and localization accuracy.

As a result, the improved results are due to the combination of two factors: 1) better penetration level and 2) planar focused wave propagation in the imaging domain. It is not

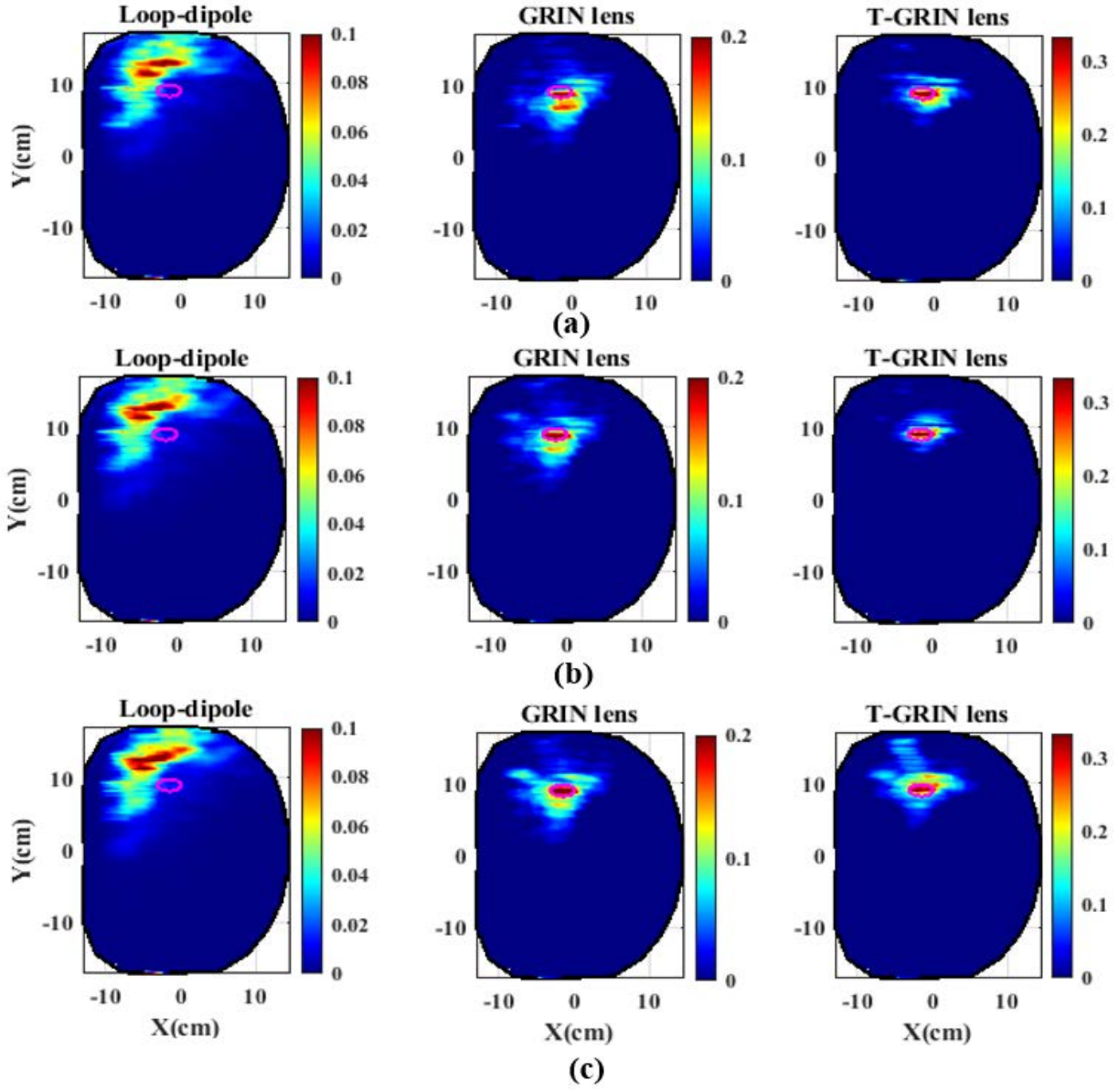

FIGURE 12. Obtained images of the numerical torso at deep target for an assumed average permittivity in the processing algorithm of (a) 40, (b) 45 (c) 50.

feasible to study each factor independently due to dependency of each one on the other one. As seen in Fig. 7, in the shallow target position, all the antennas have relatively high penetration. However, the obtained images of GRIN-lens antenna (Fig7. (b)) are better than loop-dipole antenna (Fig7. (a)) owing to the plane wave distribution inside the imaging domain. The T-GRIN lens antenna achieves focused plane wave propagation and the highest penetration depth into the torso. Hence, regardless of the employed radar-based imaging algorithm, it gives better quality images.

It should be noted the performance of antennas is comparable only in scenarios when there is a target inside the imaging domain. It is observed that in non-target scenario, all antennas generated almost similar images.

1) EFFECT OF AVERAGE PERMITTIVITY

Like all confocal radar-based imaging technique, DMAS method requires an assumption of the average effective permittivity of the medium as a priori information. As discussed in Sec III, the value of the average permittivity is set to 45, the accumulation of fat between organs and tissues in obese people can change the average effective permittivity of the torso. Hence, reliability of the conclusions in this investigation to the assumed average permittivity of the imaging domain should be evaluated.

The image of each setup at deep target location is reconstructed by changing the assumed average permittivity in the algorithm. Fig. 12 shows the obtained images from different antennas at deep target location by assuming average

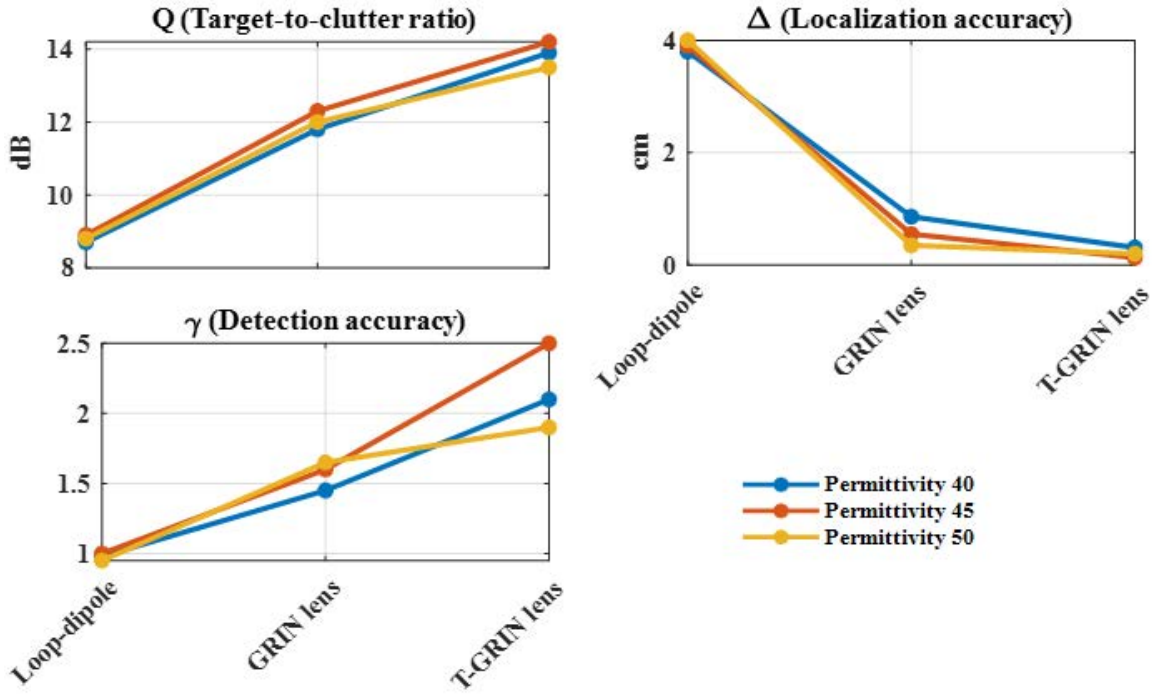

FIGURE 13. Qualitative analysis of obtained images using different antennas with the assumption of different average permittivity values in the processing algorithm.

permittivity of the imaging domain as 50, 45, and 40. Visually, it seems that the accuracy of detection is not affected significantly for different values of the assumed permittivity.

To verify this observation, the quantitative metrics are calculated for the obtained images and presented in Fig. 13. The results indicate a slight negative impact on accuracy of detection and localization. Nevertheless, the T-GRIN lens antenna still gives the best results compared to other types of antennas.

TABLE 2. The mixing ratio of water and glycerin for tissue-mimicking mixtures.

TISSUE TYPE	GLYCERIN	WATER
Lung	67%	33%
Liver	38%	62%
Average	39.5%	60.5%

2) EFFECT OF NOISE

To investigate the effect of noise on accuracy of obtained images, white Gaussian noise with different levels of power is added to the collected simulated signals of the deep target as an example from each antenna setup to emulate different signal- to-noise ratios (SNR) changing from 10 dB to 30 dB. The obtained images are depicted in Fig 14. Visual inspection reveals that decreasing SNR results more clutters and ghost/false positive targets to the images. However, the T-GRIN lens antenna is the only one that can detect the target accurately even in a noisy condition (SNR $=$ 10 dB). Additionally, its images are less affected by clutters compared to other antennas. To verify this observation, the quantitative metrics are used to assess the obtained images and the results are presented in Fig. 15. The T-GRIN lens antenna obviously gives better images and is thus more robust to noise than other antennas. While the GRIN lens antenna can faintly hint to the location of the target, the T-GRIN lens antenna is the only one that can detect and localize accurately ($\gamma > 1$) even in SNR $=$ 10 dB. The others fail to detect the target in a noisy environment.

B. EXPERIMENTAL SETUPS

To verify the effect of focused plane wave propagation on detection and localization, each of the three antennas is used to image a 3-D printed phantom, which consists of skin, fat, liver and lungs. The rest of torso tissues including muscle are represented by an average mixture that has permittivity of 45 at 1 GHz. As shown in Fig 16(a), due to the limitations of the Selective Laser Sintering (SLS) 3D printing machine, each half of torso's shell and internal organs are printed using polymethyl-methacrylate acrylic (PMMA) plastic with permittivity of 3.5 at 1GHz on two separate sides. This material has a dielectric property close to the actual fat tissue. Then, each pair is glued together and sealed with waterproof epoxy to form the 3-D phantom. Finally, the phantom is covered by a polymer-based mimicking skin tissue that is composed of epoxy resin reinforced with graphite and aluminium

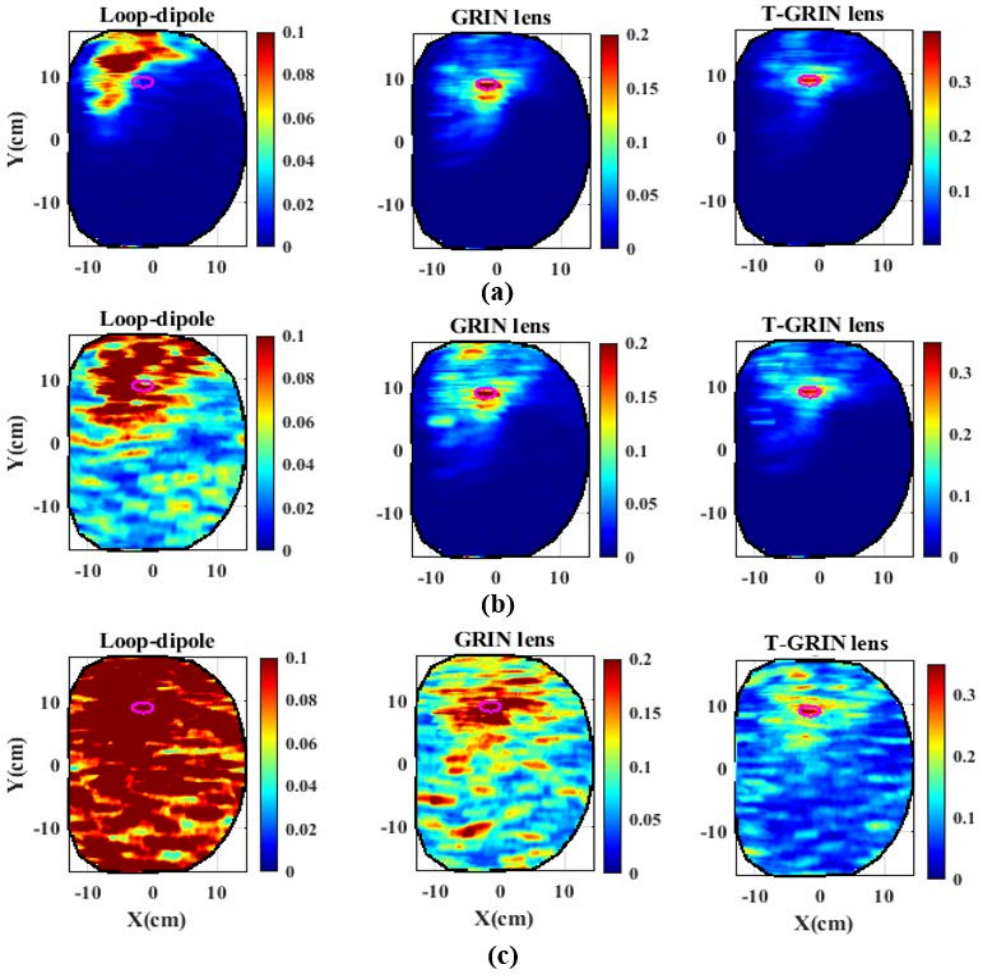

FIGURE 14. Obtained images of the numerical torso for a deep target with SNR of (a) 30 dB (b) 20 dB (c) 10 dB.

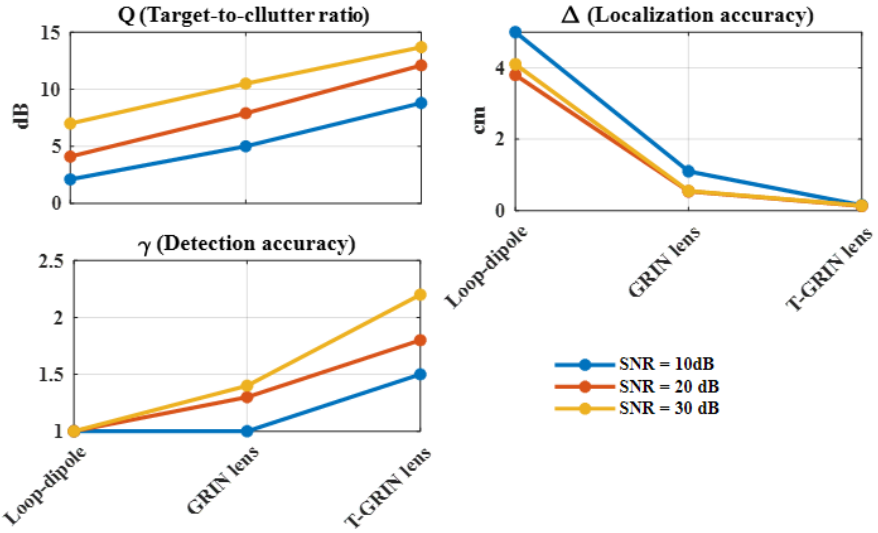

FIGURE 15. Qualitative analysis of obtained images using different antennas for different values of SNR.

oxide [35]. Different tissue-mimicking mixtures representing the dielectric properties of the average torso tissues, lungs, and liver, as presented in Table 1, are prepared using different ratios of glyceride and water as explained in [35]. The percentage of the components in each fabricated mixture is presented in Table 2. The verification of dielectric

property of these mixtures are comprehensively discussed in [35]. Liver and lungs are filled with corresponding mixture via proper tubes at the bottom of the phantom. The volume around these tissues is filled with average torso mixture. As a result, dielectric properties of different parts of the phantom exactly mimic those of the real human tissues. This phantom provides a complex heterogenous medium similar to the human torso.

To obtain information from different angles, this phantom is mounted on a platform and rotated with 18° step intervals. Fig. 16(b) shows different type of the antennas utilized in each setup to scan the phantom. Fig. 16(c) shows sample experimental setup with the T-GRIN lens antenna. In this setup, the antenna is fixed, and the phantom is rotated to form a complete circular scan in mono-static data acquisition mode. This process is repeated for all three antennas. A matching medium with permittivity of 45 and conductivity of 0.14 at 1 GHz in a thin plastic bag is placed between the antenna and the hard-shell phantom to avoid any air-gap and deterioration in the penetration depth of the antennas. In each setup, to calibrate the signal, the torso is scanned twice. Firstly, the phantom and all tissues are filled with average torso mixture (homogenous medium), and secondly each tissue is filled with its corresponding mixture and a target that emulates pulmonary edema is inserted into the lung (non-homogenous medium). A balloon, which is filled by 10 ml distilled water, is placed inside one of the lungs to emulate pulmonary edema. The target is located in two separate deep and shallow positions. For deep position, it is located inside the right-side lung at depth x = 110 mm and y = 60 mm. For shallow position, the target is located closer to the skin surface in the left-side lung at depth x = 60 mm and y = 65 mm.

To verify accuracy of the fabricated antennas and phantom, Fig. 17 shows the measured reflection coefficients ($|S_{11}|$) of the utilized antennas in front of the phantom compared to the simulated results. They agree well indicating accuracy of the experimental setup. The small discrepancies are attributed to fabrication errors and/or slight variation in the dielectric properties (conductivity or permittivity) of the emulated tissues. If tuning is needed, the main parameter that can be modified is the distance between the radiator and lens. As thoroughly discussed in [26], variation of this distance affects the impedance matching and EFI of the lens antenna. Hence, any mismatching issue can be tackled by tuning this parameter instead of the costly and time-consuming re-fabrication processes.

Fig. 18 illustrates the obtained images using the three different antennas. In comparison, the T-GRIN lens is the most efficient antenna in accurate localization and detection of deep or shallow targets. Its images also have the highest level of intensity within the imaging domain. These observations are consistent with simulation outcomes.

The three quantitative metrics are used to assess quality of images obtained from each antenna, and the results are presented in Fig. 19. In deep target scenario, the images from the T-GRIN are enhanced in target-to clutter-ratio by 11%, and 46.8% and in detection accuracy by 22.2% and 33.3% with respect to conventional GRIN-lens and loop-dipole, respectively. Additionally, in shallow target scenario, the

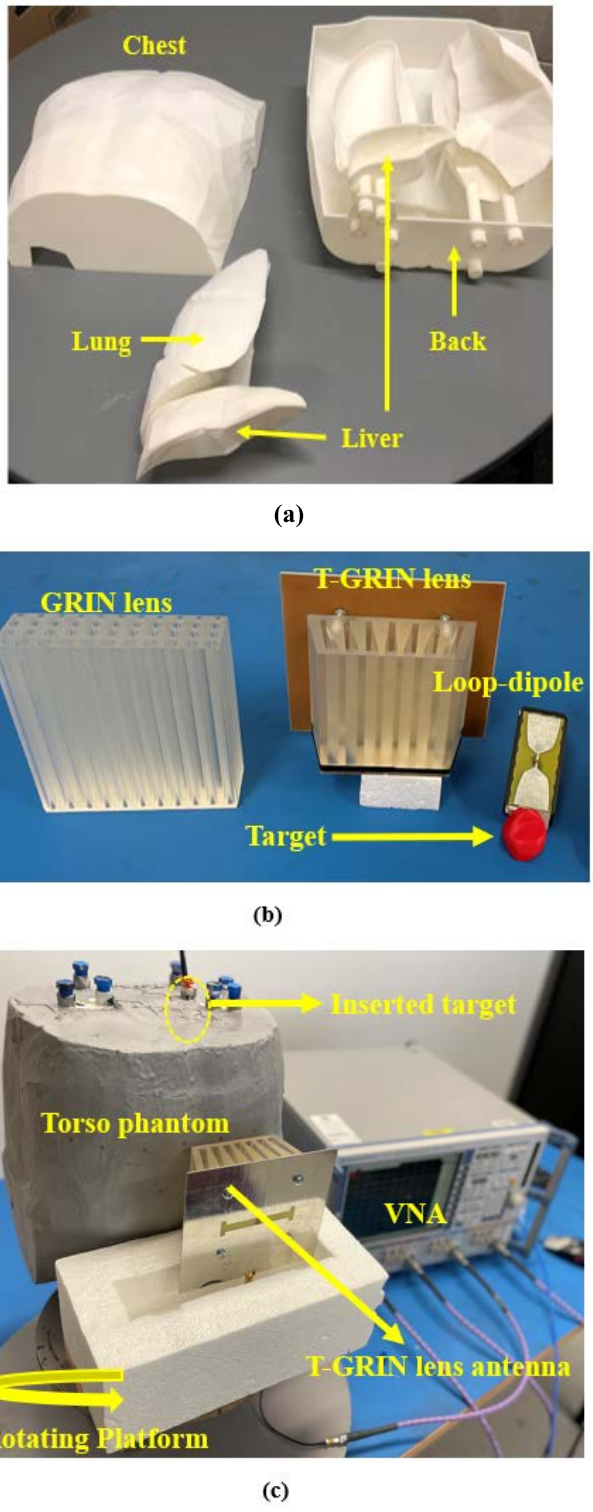

FIGURE 16. (a) 3-D printed phantom, liver, and lungs. (b) Three different utilized antennas to scan the phantom. Target is 10 ml accumulated distilled water in a balloon. (c) Experimental setup utilizing T-GRIN lens antenna as transducer.

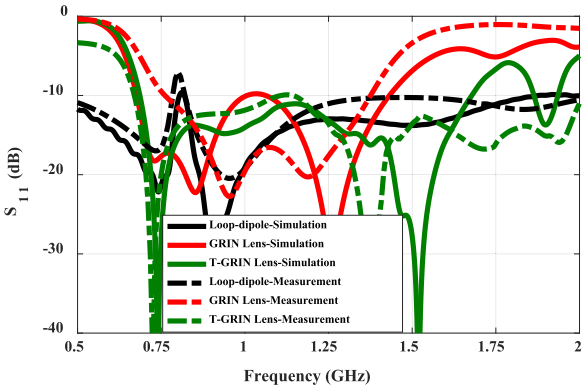

FIGURE 17. Comparison of measured $|S_{11}|$ between loop-dipole, GRIN lens and T- GRIN lens antennas in measurement and simulation.

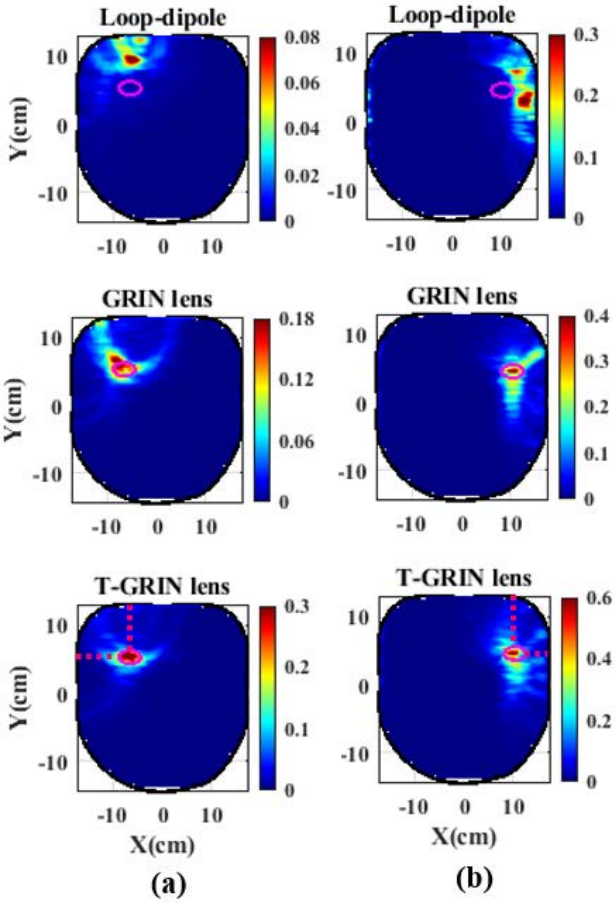

FIGURE 18. Obtained experimental images with (a) deep and (b) shallow target locations using different types of antennas.

T-GRIN lens achieves an average of 33.3% higher target-to-clutter ratio and 41.3% detection accuracy compared to other antennas. Moreover, the localization accuracy of T-GRIN lens antenna is enhanced by 25% and 87.5% compared to conventional GRIN lens in shallow and deep target scenarios, respectively. This enhanced localization accuracy is contributed to the focused high intensity incident field distribution that suppresses clutter from surrounding tissues.

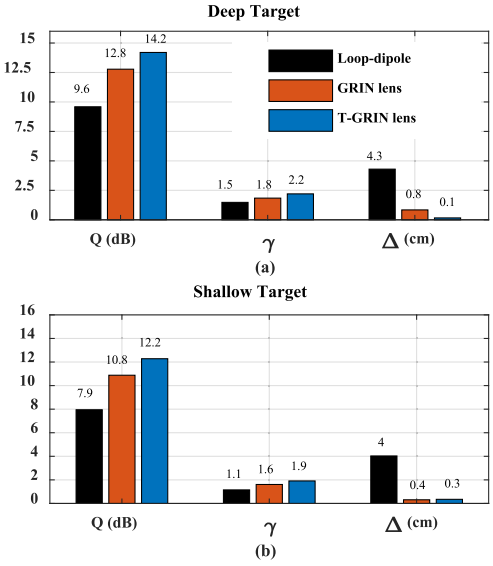

FIGURE 19. Qualitative comparison of obtained experimental images using different antennas for (a) deep and (b) shallow targets.

V. CONCLUSION

The effects of using focused planar wave front within the near-field microwave imaging domain on detection and localization accuracy have been investigated. The results demonstrate that the distribution of fields and penetration depth of those fields have significant effect on detection and localization. Antennas that can achieve focused planar wave front and high penetration depth into the imaging domain can significantly improve imaging results. These types of antennas are more immune to clutter, noise and errors in any priori assumption needed in processing algorithms. To fulfil these requirements, a T-GRIN lens antenna is designed, fabricated, and successfully tested in a realistic torso imaging setup as an example. The only limitation of the presented antenna is its large size that makes it challenging to build arrays for setups that operate in a multistatic data collection mode. However, owing to its focused planar wave front and high penetration depth, this antenna is a suitable candidate in monostatic data collection mode where one rotating antenna scans the imaging domain.

REFERENCES

[1] H. B. Lim, N. T. T. Nhung, E.-P. Li, and N. D. Thang, "Confocal microwave imaging for breast cancer detection: Delay-multiply-and-sum image reconstruction algorithm," *IEEE Trans. Biomed. Eng.*, vol. 55, no. 6, pp. 1697–1704, Jun. 2008, doi: 10.1109/TBME.2008.919716.

[2] N. Celik, R. Gagarin, G. C. Huang, M. F. Iskander, and B. W. Berg, "Microwave stethoscope: Development and benchmarking of a vital signs sensor using computer-controlled phantoms and human studies," *IEEE Trans. Biomed. Eng.*, vol. 61, no. 8, pp. 2341–2349, Aug. 2014, doi: 10.1109/TBME.2013.2241763.

[3] O. J. Babarinde and M. F. Jamlos, "UWB microwave imaging for lung tumor detection in a thorax model," in *Proc. IEEE Symp. Wireless Technol. Appl. (ISWTA)*, Sep. 2014, pp. 130–133.

[4] W. Ameer, D. Awan, S. Bashir, and A. Waheed, "Use of directional UWB antenna for lung tumour detection," in *Proc. 2nd Int. Conf. Advancements Comput. Sci. (ICACS)*, Feb. 2019, pp. 1–5.

[5] A. Alhawari, "Lung tumour detection using ultra-wideband microwave imaging approach," *J. Fundam. Appl. Sci.*, vol. 10, no. 2, pp. 222–234, 2018.

[6] S. Mustafa, B. Mohammed, and A. Abbosh, "Novel preprocessing techniques for accurate microwave imaging of human brain," *IEEE Antennas Wireless Propag. Lett.*, vol. 12, pp. 460–463, 2013, doi: 10.1109/LAWP.2013.2255095.

[7] E. C. Fear, J. Bourqui, C. Curtis, D. Mew, B. Docktor, and C. Romano, "Microwave breast imaging with a monostatic radar-based system: A study of application to patients," *IEEE Trans. Microw. Theory Techn.*, vol. 61, no. 5, pp. 2119–2128, May 2013, doi: 10.1109/TMTT.2013.2255884.

[8] D. Byrne and I. J. Craddock, "Time-domain wideband adaptive beamforming for radar breast imaging," *IEEE Trans. Antennas Propag.*, vol. 63, no. 4, pp. 1725–1735, Apr. 2015, doi: 10.1109/TAP.2015.2398125.

[9] M. O'Halloran, E. Jones, and M. Glavin, "Quasi-multistatic MIST beamforming for the early detection of breast cancer," *IEEE Trans. Biomed. Eng.*, vol. 57, no. 4, pp. 830–840, Apr. 2010, doi: 10.1109/TBME.2009.2016392.

[10] Y. Xie, B. Guo, L. Xu, J. Li, and P. Stoica, "Multistatic adaptive microwave imaging for early breast cancer detection," *IEEE Trans. Biomed. Eng.*, vol. 53, no. 8, pp. 1647–1657, Aug. 2006, doi: 10.1109/TBME.2006.878058.

[11] N. Ghavami, G. Tiberi, D. J. Edwards, and A. Monorchio, "Microwave imaging through a mode-matching Bessel functions procedure," *IEEE Trans. Microw. Theory Techn.*, vol. 61, no. 8, pp. 2753–2760, Aug. 2013, doi: 10.1109/TMTT.2013.2271612.

[12] R. Chandra, A. J. Johansson, M. Gustafsson, and F. Tufvesson, "A microwave imaging-based technique to localize an in-body RF source for biomedical applications," *IEEE Trans. Biomed. Eng.*, vol. 62, no. 5, pp. 1231–1241, May 2015.

[13] A. Darvazehban, S. A. Rezaeieh, and A. Abbosh, "Pattern-reconfigurable loop–dipole antenna for electromagnetic pleural effusion detection," *IEEE Trans. Antennas Propag.*, vol. 68, no. 8, pp. 5955–5964, Aug. 2020, doi: 10.1109/TAP.2020.2987434.

[14] N. Khaltaev and S. Axelrod, "Chronic respiratory diseases global mortality trends, treatment guidelines, life style modifications, and air pollution: Preliminary analysis," *J. Thoracic Disease*, vol. 11, no. 6, p. 2643, 2019.

[15] P. Rocca, M. Benedetti, M. Donelli, D. Franceschini, and A. Massa, "Evolutionary optimization as applied to inverse scattering problems," *Inverse Problems*, vol. 25, no. 12, pp. 1–41, Dec. 2009.

[16] S. Caorsi, A. Massa, and M. Pastorino, "A computational technique based on a real-coded genetic algorithm for microwave imaging purposes," *IEEE Trans. Geosci. Remote Sens.*, vol. 38, no. 4, pp. 1697–1708, Jul. 2000.

[17] A. E. Souvorov, "Microwave tomography: A two-dimensional Newton iterative scheme," *IEEE Trans. Microw. Theory Techn.*, vol. 46, no. 11, pp. 1654–1659, Nov. 1998.

[18] J. D. Zaeytijd, A. Franchois, C. Eyraud, and J.-M. Geffrin, "Full-wave three-dimensional microwave imaging with a regularized Gauss–Newton method—Theory and experiment," *IEEE Trans. Antennas Propag.*, vol. 55, no. 11, pp. 3279–3292, Nov. 2007.

[19] P. Mojabi and J. LoVetri, "Overview and classification of some regularization techniques for the Gauss-Newton inversion method applied to inverse scattering problems," *IEEE Trans. Antennas Propag.*, vol. 57, no. 9, pp. 2658–2665, Sep. 2009, doi: 10.1109/TAP.2009.2027161.

[20] X. Li, *Body Matched Antennas for Microwave Medical Applications*. Karlsruhe, Germany: KIT Scientific Publishing, 2014.

[21] J. Blauert and A. Kiourti, "Bio-matched antennas with flare extensions for reduced low frequency cutoff," *IEEE Open J. Antennas Propag.*, vol. 1, pp. 136–141, 2020, doi: 10.1109/OJAP.2020.2988133.

[22] H. Zhang, M. Li, F. Yang, S. Xu, H. Zhou, Y. Yang, and L. Chen, "A low-profile compact dual-band L-shape monopole antenna for microwave thorax monitoring," *IEEE Antennas Wireless Propag. Lett.*, vol. 19, no. 3, pp. 448–452, Mar. 2020, doi: 10.1109/LAWP.2020.2967142.

[23] B. Biswas, R. Ghatak, and D. R. Poddar, "A fern fractal leaf inspired wideband antipodal Vivaldi antenna for microwave imaging system," *IEEE Trans. Antennas Propag.*, vol. 65, no. 11, pp. 6126–6129, Nov. 2017, doi: 10.1109/TAP.2017.2748361.

[24] A. Darvazehban, S. A. Rezaeieh, and A. M. Abbosh, "Programmable metasurface antenna for electromagnetic torso scanning," *IEEE Access*, vol. 8, pp. 166801–166812, 2020, doi: 10.1109/ACCESS.2020.3022870.

[25] A. Darvazehban, S. A. Rezaeieh, O. Manoochehri, and A. M. Abbosh, "Two-dimensional pattern-reconfigurable cross-slot antenna with inductive reflector for electromagnetic torso imaging," *IEEE Trans. Antennas Propag.*, vol. 68, no. 2, pp. 703–711, Feb. 2020, doi: 10.1109/TAP.2019.2940617.

[26] S. A. Rezaeieh, A. Darvazehban, M. Khosravi-Farsani, and A. M. Abbosh, "Body-matched gradient index lens antenna for electromagnetic torso scanner," *IEEE Trans. Antennas Propag.*, vol. 69, no. 10, pp. 6165–6174, Oct. 2021, doi: 10.1109/TAP.2021.3061593.

[27] A. K. Baghel, S. S. Kulkarni, and S. K. Nayak, "Far-field wireless power transfer using GRIN lens metamaterial at GHz frequency," *IEEE Microw. Wireless Compon. Lett.*, vol. 29, no. 6, pp. 424–426, Jun. 2019, doi: 10.1109/LMWC.2019.2912056.

[28] Y. He and G. V. Eleftheriades, "Matched, low-loss, and wideband graded-index flat lenses for millimeter-wave applications," *IEEE Trans. Antennas Propag.*, vol. 66, no. 3, pp. 1114–1123, Mar. 2018, doi: 10.1109/TAP.2018.2790173.

[29] K. V. Hoel and S. Kristoffersen, "Characterization of variable density 3D printed materials for broadband GRIN lenses," in *Proc. IEEE Int. Symp. Antennas Propag. USNC/URSI Nat. Radio Sci. Meeting*, Jul. 2017, pp. 2643–2644, doi: 10.1109/APUSNCURSINRSM.2017.8073364.

[30] S. Zhang, Y. Vardaxoglou, W. Whittow, and R. Mittra, "3D-printed graded index lens for RF applications," in *Proc. Int. Symp. Antennas Propag. (ISAP)*, Oct. 2016, pp. 90–91.

[31] H. Xin and M. Liang, "3-D-printed microwave and THz devices using polymer jetting techniques," *Proc. IEEE*, vol. 105, no. 4, pp. 737–755, Apr. 2017, doi: 10.1109/JPROC.2016.2621118.

[32] N. Bayat and P. Mojabi, "The effect of antenna incident field distribution on microwave tomography reconstruction," *Prog. Electromagn. Res.*, vol. 145, pp. 153–161, 2014.

[33] N. Bayat and P. Mojabi, "On the use of focused incident near-field beams in microwave imaging," *Sensors*, vol. 18, no. 9, p. 3127, Sep. 2018. [Online]. Available: https://www.mdpi.com/1424-8220/18/9/3127

[34] *Tissue Properties Database, the Foundation for Research on Information Technologies in Society (IT'IS)*. Accessed: Apr. 1, 2021. [Online]. Available: https://itis.swiss/virtual-population/tissue-properties/database/tissue-frequency-chart/

[35] S. A. Rezaeieh, A. Brankovic, A. S. Janani, B. Mohammed, A. Darvazehban, A. Zamani, G. A. Macdonald, and A. M. Abbosh, "Wearable electromagnetic belt for steatotic liver detection using multivariate energy statistics," *IEEE Access*, vol. 8, pp. 201847–201860, 2020.

[36] W. Chew, *Waves Fields Inhomogeneous Media*. Hoboken, NJ, USA: Wiley, 1990.

[37] Z. L. Mei, J. Bai, and T. J. Cui, "Gradient index metamaterials realized by drilling hole arrays," *J. Phys. D, Appl. Phys.*, vol. 43, no. 5, Feb. 2010, Art. no. 055404.

[38] D. Cook *et al.*, "Case report: Preliminary images from an electromagnetic portable brain scanner for diagnosis and monitoring of acute stroke," *Front. Neurol.*, vol. 12, no. 765412, pp. 1–7, Oct. 2021, doi: 10.3389/fneur.2021.765412.

[39] L. Guo, N. Nguyen-Trong, A. AI-Saffar, A. Stancombe, K. Bialkowski, and A. Abbosh, "Calibrated frequency-division distorted born iterative tomography for real-life head imaging," *IEEE Trans. Med. Imag.*, vol. 41, no. 5, pp. 1087–1103, May 2022, doi: 10.1109/TMI.2021.3132000.

[40] O. M. Bucci and T. Isernia, "Electromagnetic inverse scattering: Retrievable information and measurement strategies," *Radio Sci.*, vol. 32, no. 6, pp. 2123–2137, Nov. 1997, doi: 10.1029/97RS01826.

[41] A. Zamani, A. M. Abbosh, and S. Crozier, "Multistatic biomedical microwave imaging using spatial interpolator for extended virtual antenna array," *IEEE Trans. Antennas Propag.*, vol. 65, no. 3, pp. 1121–1130, Mar. 2017, doi: 10.1109/TAP.2016.2647584.

[42] A. Zamani and A. Abbosh, "Hybrid clutter rejection technique for improved microwave head imaging," *IEEE Trans. Antennas Propag.*, vol. 63, no. 11, pp. 4921–4931, Nov. 2015.

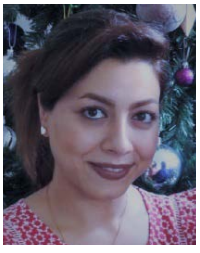

AZIN S. JANANI received the B.S. and M.S. degrees in biomedical engineering from Amirkabir University (Tehran Poly-Technique), Iran, in 2008 and 2010, respectively, and the Ph.D. degree from Flinders University, Australia, in 2019. She joined the Electromagnetic Research Group, The University of Queensland, as a Postdoctoral Fellow, in 2019. Her research interests include signal processing, disease classification, and computer aided diagnosis system development. She was a recipient of the Australian Endeavour Postgraduate Scholarship, in 2016, for her Ph.D. studies.

AMIN DARVAZEHBAN (Member, IEEE) received the B.Sc. degree in electrical engineering from Shahid Beheshti University, Tehran, Iran, in 2011, the M.S. degree from the Amirkabir University of Technology, Tehran, in 2013, and the Ph.D. degree from The University of Queensland, Brisbane, QLD, Australia, in 2021.

He was a Researcher with the Electromagnetic and Nondestructive Testing Laboratory, Amirkabir University of Technology, from 2013 to 2017. He is currently a Postdoctoral Research Fellow with the Electromagnetic Innovations ($\mathcal{E}$MAGin) Group, School of Information Technology and Electrical Engineering, The University of Queensland. His current research interests include the design of various miniaturized biomedical antennas and systems, the development of clinical biomedical platforms beam forming networks, metasurfaces, pattern reconfigurable antennas, and passive microwave devices.

SASAN AHDI REZAEIEH (Member, IEEE) received the Ph.D. degree from The University of Queensland, Brisbane, QLD, Australia, in 2016, with a focus on design of electromagnetic torso scanner systems. His current research interests include design and miniaturization of several types of metamaterial, metasurface, and pattern reconfigurable antennas for electromagnetic medical diagnostic systems. He was a recipient of the IEEE Antennas and Propagation Society Doctoral Research Award, in 2014, the IEEE Antennas and Propagation Letters Outstanding Reviewer Award, in 2018, and the Prestigious Advance Queensland Fellowship jointly funded by the Queensland Government, Australia, and The University of Queensland.

AMIN M. ABBOSH (Fellow, IEEE) received the Doctor of Engineering degree from The University of Queensland, Australia, in 2013. He leads the Electromagnetic Innovations ($\mathcal{E}$MAGin) Group, The University of Queensland. He has authored more than 400 papers on electromagnetic imaging systems, wideband passive microwave devices, and planar antennas. He won IEEE APS King Prize Paper Award twice.